Case Study

Oso, Washington, Landslide of March 22, 2014: Dynamic Analysis

Jordan Aaron[1]; Oldrich Hungr[2]; Timothy D. Stark, F.ASCE[3]; and Ahmed K. Baghdady, S.M.ASCE[4]

Abstract: This paper describes and explains the spectacular mobility of the 2014 Oso landslide, which was the cause of its fatal consequences. A geomorphic interpretation of the site conditions is used to reconstruct the landslide failure mechanism. Two numerical models are used to conduct an inverse runout analysis. The models implement a newly defined rheology appropriate for liquefied soils. It is shown that this landslide occurred in two phases, characterized by different material strengths. Although the temporal sequencing of the two phases remains somewhat ambiguous, it is clear that the distal phase underwent significant undrained strength loss (liquefaction) and travelled more than 1.4 km over a nearly horizontal surface. The proximal phase underwent brittle failure, with much less strength loss than the first phase. The parent material forming the slide mass was composed of insensitive, overconsolidated glaciolacustrine silt and clay, material not traditionally recognized as liquefiable. It is hypothesized that a substantial volume of liquefaction-prone soil was formed by colluvial softening of the parent material during the process of slope development prior to 2014. **DOI:** [10.1061/(ASCE)GT.1943-5606.0001748](https://doi.org/10.1061/(ASCE)GT.1943-5606.0001748). *© 2017 American Society of Civil Engineers.*

Introduction

On March 22, 2014 a terrace slope located northeast of Oso in the state of Washington failed catastrophically. The resulting flowslide killed 43 people in the small community of Steelhead Haven and buried Washington Highway SR 530. The slope on which the landslide originated had failed multiple times in the past at lower elevations, most recently in 2006, and had a thick accumulation of landslide debris on its surface and at its toe. In comparison with the previous failures, the March 2014 event initiated at a higher elevation, was extremely mobile, and projected debris across the width of the valley floor, causing the noted death and damage. Understanding the causes of this rapid movement is an important step in recognizing and preventing future disasters in similar settings. A related paper by Stark et al. (2017) examines the initiation and failure mechanisms of the slide, whereas this paper concentrates on the runout mechanism.

The pre-2014 landslides that occurred at this and other locations in the Stillaguamish Valley have been studied; however, most of this work focused on landslide-induced turbidity in the Stillaguamish River and its impact on fish populations (Miller 1999; Shannon and Wilson 1952). These investigations recognized two main types of landslides that occurred at the site. The first was compound sliding and motion of intact blocks, an example of which is the 1967 landslide (Miller 1999). The second type was small-volume flowlike landslides with moderate velocities, similar to earthflows. Both Miller (1999) and Shannon and Wilson (1952) attributed such flows to the disintegration of failed glaciolacustrine blocks. The landslides detailed in these reports were all small compared with the volume and impact area of the 2014 landslide and much less mobile. The most mobile of these previous failures occurred in 1967 and resulted in a temporary damming of the river channel (Miller 1999).

The 2014 flowslide represents a distinct mechanistic change in the failure behavior of this terrace slope (the terrace is referred to herein as the Whitman Bench). The failure travelled more than 1.4 km on a nearly horizontal runout surface and exhibited behavior typical of flowslides in liquefiable granular material or sensitive clay (Hungr et al. 2014). Flowslides occur in liquefiable materials that have certain specific characteristics, including low density and a high degree of saturation or high sensitivity. Based on site investigations performed before and after the flowslide, such materials were not identified at this site (Stark et al. 2017). After the 2014 landslide, it was unclear how a landslide that took place primarily in overconsolidated, insensitive glaciolacustrine silt and clay could transform into a flowslide, as evidenced by the greatly varying failure mechanisms proposed by others (Keaton et al. 2014; Iverson et al. 2015; Wartman et al. 2016; Iverson and George 2016). Nevertheless, the occurrence of extreme undrained strength loss/liquefaction is clearly implied by the observed dynamic behavior of the event.

This paper simulates the dynamics of the landslide motion with an analysis validated by field observations, remote sensing data, a reconstruction of the rupture surface of the flowslide, and an interpretation of the morphology of the landslide debris along the slope toe. An analysis is performed using two dynamic models, *DANW* and *DAN3D* (Hungr and McDougall 2009), that were modified to account for the hypothesized mechanical behavior of liquefied soils. The analysis is used to constrain the shear resistance properties necessary to reproduce field observations. Based on this, the paper suggests two alternative mechanisms that account for the unexpected and spectacular mobility of this event. The paper also

[1]Ph.D. Student, Dept. of Earth, Ocean and Atmospheric Sciences, Univ. of British Columbia, 2207 Main Mall, Vancouver, BC, Canada V6T 1Z4 (corresponding author). E-mail: jaaron@eos.ubc.ca

[2]Emeritus Professor, Dept. of Earth Ocean and Atmospheric Sciences, Univ. of British Columbia, 2207 Main Mall, Vancouver, BC, Canada V6T 1Z4. E-mail: ohungr@eos.ubc.ca

[3]Professor, Dept. of Civil and Environmental Engineering, Univ. of Illinois, 205N Mathews Ave., Urbana, IL 61801-2352. E-mail: tstark@illinois.edu

[4]Ph.D. Student, Dept. of Civil and Environmental Engineering, Univ. of Illinois, 205N Mathews Ave., Urbana, IL 61801-2352. E-mail: baghdad2@illinois.edu

© ASCE   05017005-1   J. Geotech. Geoenviron. Eng.

J. Geotech. Geoenviron. Eng., 2017, 143(9): 05017005

proposes a process of colluvium softening, which is capable of inducing high sensitivity in a portion of the source volume.

Site Overview

The Oso landslide is situated within the northern Cascade Range physiographic province. The site stratigraphy was mapped by Dragovich et al. (2003) and consists of an unusually thick glacio-lacustrine silt and clay unit overlain by advance outwash sand. The advance outwash unit is overlain by lodgement till, which in turn is covered by recessional outwash of gravel and sand. Fig. 1 shows a simplified stratigraphic section through the prelandslide topography. A more in-depth discussion of site stratigraphy is presented in Stark et al. (2017).

In 2006, a significant compound sliding failure occurred on the slope. This failure blocked the Stillaguamish River and prompted the installation of erosion protection measures at the toe of the slope by the U.S. Army Corps of Engineers. Comparison of 2003 and 2013 LiDAR images revealed a large accumulation of failed material at the toe of the slope during this period, which was augmented by the 2006 landslide. Stark et al. (2017) concluded that the accumulated colluvium from the previous landslides along the slope toe played a significant role in the spectacular mobility of the 2014 landslide.

Previous Work

The 2014 Oso flowslide has been the subject of other investigations as described in the previous section. Keaton et al. (2014) provided an overview of the meteorological conditions in the time leading up to failure, as well as site history, geomorphology, and stratigraphy. Keaton et al. (2014), based on field observations and an interpretation of the seismic signals generated by the flowslide, concluded that the 2014 landslide had a deep-seated circular failure mechanism that extended to the slope toe and river. The failure was interpreted to occur in two distinct phases of similar magnitude, separated by several minutes. The phase involving the distal part of the landslide source was assumed to have occurred first (Phase A), whereas the second phase was a later retrogressive failure extending beyond the crest of the Whitman Bench (Phase B) (Keaton et al. 2014; Hibert et al. 2015).

Iverson et al. (2015), using a different interpretation of the seismic records, proposed that the landslide occurred mainly in a single, dominant phase of motion. Iverson et al. (2015) also provided a dynamic analysis of the Oso landslide using the runout model D-CLAW. This analysis was performed based on the assumption that the material properties of the entire source volume were those of a homogeneous, loose, saturated, and liquefiable granular soil. The analysis used a novel advanced coupled strain and hydrodynamic algorithm capable of simulating pore-pressure response in a shearing granular mixture. It was found, unsurprisingly, that the simulated runout was highly sensitive to the assumed initial density of the material (represented by solid volume fraction in the analysis). Iverson et al. (2015) also noted a sharp bifurcation in the runout behavior of the material at a threshold porosity value, which is a well-known characteristic of liquefaction-prone granular soils.

Data Sources

The Oso flowslide was well documented through the authors' site visits, multiple field surveys, aerial photo imagery, and high-quality topographic data. LiDAR surveys of the valley were conducted in 2003, 2013, and immediately following the 2014 event. Aerial photo imagery of the slope is available dating back as far as the 1920s, and many pre-event and postevent oblique images are available. Both Keaton et al. (2014) and Iverson et al. (2015) documented many features of the debris field and source area, providing valuable information that aided in the present reconstruction of the event dynamics. A detailed site investigation including multiple deep exploration drill holes, some of which intercepted the rupture surface of the 2014 slide, became available to the authors in 2016 (Badger 2015). All these data sources, as well as additional data gathered during a three-day field visit by the authors in 2014, were used to guide the present analysis.

Analysis of Landslide Mechanism

The authors hypothesized that the landslide comprised two types of material. The first type consisted of the saturated colluvial accumulation (henceforth the colluvium) situated on and immediately in front of the lower slopes of the terrace as a result of a number of past slope movements which occurred on the slope over a long period. The colluvium was assumed to have experienced a large undrained strength loss during the failure and was assigned
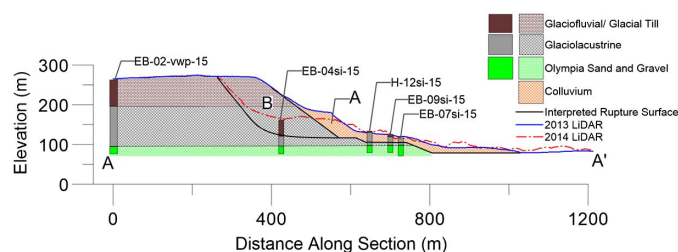
Fig. 1. Simplified stratigraphic section through the 2014 Oso landslide showing the borehole results presented by Badger (2015); the materials comprising Phases A and B are indicated; the solid line shows the proposed rupture surface, which agrees with available borehole data and surface observations; the locations of the two intermediate scarps correspond to observed prefailure scarps, and the depth of the rupture surface was determined from borehole data; the location of the boreholes and section line are shown in Fig. 2
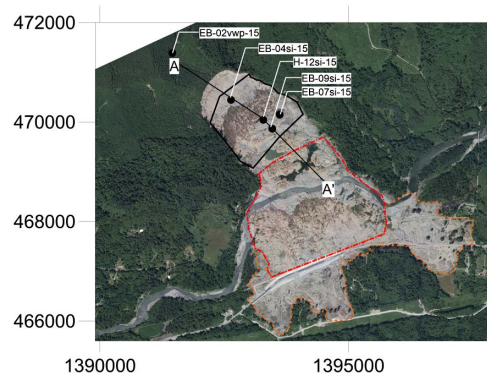
Fig. 2. Landslide zones for dynamic analyses: the dashed line outlines the splash zone, the dash-dot line outlines the valley floor deposit, and the solid line outlines the source zone; the locations of the boreholes used to constrain the rupture surface are shown (background image courtesy of Esri Disaster Response Program and WSDOT)

© ASCE 05017005-2 J. Geotech. Geoenviron. Eng.

J. Geotech. Geoenviron. Eng., 2017, 143(9): 05017005

a correspondingly low shear strength in the dynamic analysis. The second material included the intact glaciofluvial and glaciolacustrine soils of the upper slopes (henceforth *the intact soils*). The intact soil was considered to be a frictional material with moderate pore-water pressures because of its relatively high density and incomplete saturation. The selection of strength parameters for the intact soils was guided by laboratory tests summarized in Stark et al. (2017). Further discussion of the characteristics of the two materials follows.

Testing the hypothesis that the colluvium liquefied is difficult using conventional geotechnical analyses. This material was composed of large blocks of overconsolidated clay, surrounded by a matrix of mixed softened and saturated soil produced by mechanical disturbance of the parent material. Its undrained behavior was likely influenced by extreme heterogeneity and by macroscopic interactions between intact blocks and the fluid matrix. Testing such a material using field or laboratory analysis is very difficult and has not been attempted. Instead, the authors used inverse analysis of landslide motion to constrain the shear strength properties acting during failure. An inverse analysis of the 2014 failure was performed using two dynamic models: DANW, which simulates landslide motion in two dimensions along a cross section, and DAN3D which analyzes landslide motion over three-dimensional (3D) terrain. The two-dimensional (2D) analysis was performed first and the initial calibration was validated by the deposit thicknesses after the 2014 slide determined from the 2014 LiDAR.

The 3D DAN3D simulations were guided by the best-fit parameters obtained in the 2D analyses. The purpose of the 3D simulation was to determine the shear strength distribution required to adequately reproduce the impact area and velocities of the 2014 landslide. The 3D simulation results were verified by comparing them to field evidence of impact area, deposit thickness, and vulnerability indices.

Because this study relied on inverse analysis to infer movement mechanisms, the first step of the analysis was a detailed geomorphological interpretation of the debris field. This analysis highlighted observations of the landslide deposit that have not been previously published. This provided the constraints for the reconstruction of the rupture surface, as well as for the subsequent dynamic analysis.

As noted elsewhere in this paper, some uncertainty remains over whether the 2014 failure occurred as a single event or whether there was a time gap between the two phases of movement. Therefore both hypotheses were tested. Alternative analyses using the models were conducted treating the mass both as one event and as two temporally discrete events for comparison purposes.

Examination of Debris Field

This paper focuses on a few specific features of the debris field that were used to constrain the dynamic analysis. In particular, the trees preserved on the slide surface were correlated with the original forest on and below the Whitman Bench to reconstruct the trajectories of various parts of the deposit. For this purpose, three separate zones of the debris field are discussed: the source zone, the valley floor, and the *splash* zone (Fig. 2).

In this paper, the term *source volume* refers to the volume contained between the prefailure ground surface and the rupture surface. It is the volume of material moved by the landslide. The *deposit volume* is the volume between the final, postslide ground surface and the failure surface or preslide ground surface downhill from the source area. Usually the two volumes overlap, because some material may deposit within the source volume from
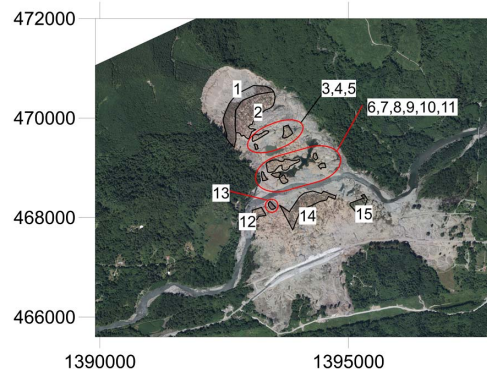
Fig. 3. Polygons of intact forest blocks in 2014 slide mass used to constrain the origin of different features of the debris; Polygons 1 and 2 have a combined area of 59,000 m², corresponding to the prefailure area of trees on the Whitman Bench (Fig. 4); Polygons 3–15 have a combined area of 50,000 m², corresponding to the area of the trees in front of the Whitman Bench (Fig. 4) (background image courtesy of Esri Disaster Response Program and WSDOT)

which it originated. In slow-moving landslides, the two volumes may strongly overlap. In a mobile event, they may be almost totally separate, divided by a *path*.

The source area is understood here as the planar footprint of the source volume. Fig. 3 shows that the proximal source area features thick deposits, consisting largely of a relatively intact but heavily internally sheared block, covered by trees (Polygons 1 and 2 in Fig. 3). Apart from a series of scarps formed by internal shears, the forest floor is mostly intact on this block. This suggests that the proximal block remained relatively coherent during its movement, although the abundance of internal shear surfaces exposed by normal offsets testifies to strong internal shear deformation and suggests nonrotational shape of the sliding surface. Allowing for some spreading, the area of the forest floor that remained intact on this block was measured to be 59,000 m². By overlaying the impact area of the 2014 landslide on a preslide orthophotograph taken in 2013, it is possible to determine where the trees present on this block must have originated. Fig. 4 shows that the intact block of trees derived from the surface of Whitman Bench located at the head of the slide and from a part of the prehistoric scarp (Polygon 16, which also has an area of 59,000 m²). The heavily forested area lying originally downslope of the Whitman Bench
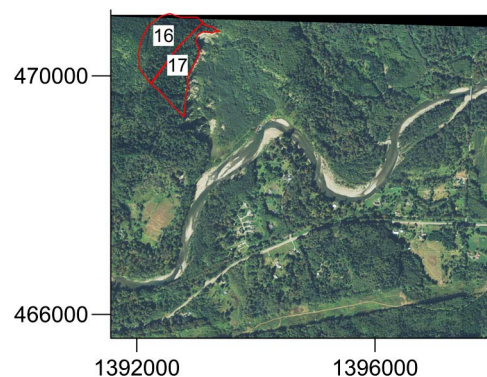
Fig. 4. Measurement of tree areas on pre-2014 orthophotograph; Polygons 16 and 17 have a measured area of 59,000 and 54,000 m², respectively (background image from National Agriculture Imagery Program, data available from the U.S. Geological Survey)

© ASCE　　　　　　　　　　　　　　05017005-3　　　　　　　　　　　　　　J. Geotech. Geoenviron. Eng.

J. Geotech. Geoenviron. Eng., 2017, 143(9): 05017005

Fig. 5. (a) Postevent image of 2014 Oso flowslide source zone with intact blocks that appear to have undergone extension while traveling over an inclined surface (see square); (b) side view of the dropped-down blocks (images by Jordan Aaron)

crest (Polygon 17) consists of an ancient slide block, likely made up of previously displaced material (Stark et al. 2017).

To the southeast of this proximal block, the landslide deposits exhibit blocks of coherent material that appear to have dropped down while moving over a sloping surface (Fig. 5). This indicates that the material forming the proximal debris deposits underwent sliding failure on a compound sliding surface, which necessitated disruption on multiple internal shear surfaces. However, in contrast to the distal deposits, there is no evidence of liquefaction in this part of the debris.

The 2014 debris that deposited on the valley floor has a much more disturbed morphology. These deposits are disaggregated and mostly consist of glaciolacustrine deposits overlain by discontinuous ridges and hummocks of sand, some of which are topped with mature trees in varying degrees of tilt. Most of this sand represents blocks from below the crest of the Whitman Bench, although some of it probably originated from sand blocks moved by previous landslides and resting originally on the upper slopes. Small rafts of intact forest floor can be found within the valley floor debris. Measuring the combined area of these relatively intact blocks (Polygons 3 through 15 in Fig. 3) and correcting for spreading (by making the assumption that these blocks were stretched by 15%) yields a total forest area of 50,000 m^2. The forest originating on the Whitman bench surface is already accounted for by the source zone deposit, so these trees must have originated from the area downslope of the Whitman bench, including the surface of the ancient slide block and the surrounding upper slopes.

The splash zone is located at the distal margins of the 2014 slide deposit (Fig. 2). Based on the accumulation/depletion map (Fig. 6) it can be seen that the deposits in this zone are extremely thin. Comparing Figs. 3 and 4 shows that some trees that originally grew on the floodplain in this zone remained standing after the 2014 slide, indicating that they resisted the impact of the fluid debris. A common feature of large landslides is a splash zone surrounding the distal end of deposits [termed a *Spritzone* by Heim (1932)]. It is likely that this area was overrun by water and highly liquid colluvium pushed in front of the main debris mass. Some of the debris in the splash zone also originated from channel and floodplain deposits entrained or pushed together with surface water from the path of the rapidly-moving flowslide front.

Based on the analysis described above, the morphology of the deposits can be summarized as follows:

- Source zone, which contains a nearly intact although heavily deformed block at the head, bordered by highly sheared but

massive blocks that appear to have travelled for a limited distance down a sloping, steplike surface from a higher elevation;
- Valley floor, which consists of widely spread fluid deposits bearing rafts of intact sand and clay; and
- Distal splash zone, which consists only of fluidized material and organic debris.

Temporal Sequence of Landslide

The temporal sequencing of the movement phases during the 2014 landslide remains ambiguous in the literature. The available seismic signals from a number of stations clearly indicate two phases of motion (Keaton et al. 2014). However, different groups of analysts have published different and strongly conflicting interpretations of the mechanism producing the signals (Iverson et al. 2015; Hibert et al. 2015).

Similarly, eyewitness records, reported in detail by the same two references, are not explicit. Some witnesses reported two events,
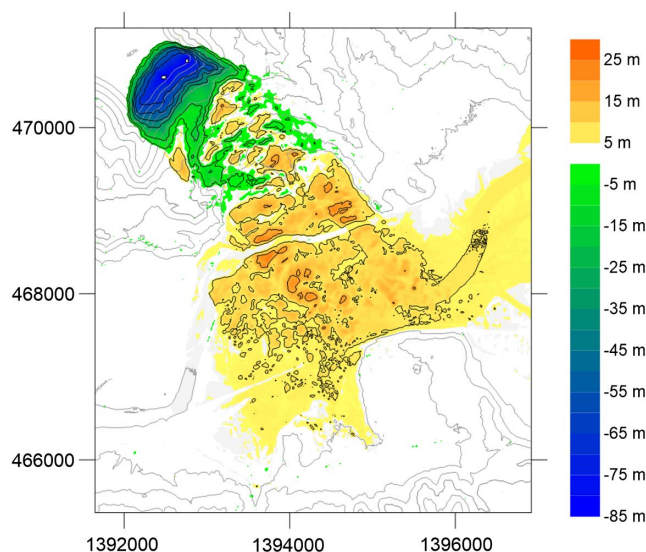
Fig. 6. Accumulation and depletion zones of 2014 Oso landslide showing that deposits in the splash zone are thin; as summarized in Keaton et al. (2014), the thin deposits extending to the northeast were due to postslide flooding

© ASCE

05017005-4

J. Geotech. Geoenviron. Eng.

others only one. None of the witnesses in these references stated explicitly that the damage to Steelhead Haven was caused by the first motion phase (Phase A) and was followed by a less mobile retrogression (Phase B). This contradicts the conclusion of Keaton et al. (2014). Iverson et al. (2015) quoted an eyewitness who claims he heard an intense sound emanating from upper slopes at a moment when the Stillaguamish River channel was still unaffected. According to this eyewitness, the landslide front reached the river some time after the initial sound.

Three possible scenarios can be considered:

1. The distal Phase A occurred first, involving mostly the colluvial deposits, although triggered by an instability of the upper part of the slope. Its high mobility caused the damage to Steelhead Haven. The retrogressive Phase B subsequently reached the present river channel but played no role in the disastrous damage (Keaton et al. 2014; Stark et al. 2017).

2. Both phases occurred simultaneously, the second seismic signal being due to a minor retrogression of the head scarp. This is an interpretation advanced by Iverson et al. (2015).

3. The proximal Phase B, consisting of a very deep, compound sliding failure of the crest of the Whitman Bench, occurred first, having been triggered by a pore-pressure increase on a weak layer in the stratigraphy. This failure emitted the sound heard by the eyewitness mentioned previously and produced the first seismic signal. Due to its limited mobility, the toe of this failure did not reach the river, but daylighted on the lower midslope. The weight of the slide mass caused rapid loading and deformation of the colluvial accumulations covering the lower slopes. After a short time, during which strains and pore-pressures readjusted within the slope, the large colluvial mass on the lower slopes failed. This failure was accompanied by spontaneous liquefaction of the softened colluvium, and the mobile, destructive Phase A took place, crashing into and displacing the river, covering Steelhead Haven with flowslide debris, and displacing a *splash* of watery debris to the distal margins of the damage zone.

From a mechanistic point of view, supported by the dynamic analyses reported subsequently, the exact sequence of movement is not very important. What is important is to determine the source of the energy that projected the damaging landslide front to the south bank of the river. Certainly, a huge store of potential energy was represented by the high slope of the Whitman Bench in the proximal part of the source volume. However, this area was also a zone of non-liquefaction-prone debris, which had the capacity to absorb correspondingly large amounts of energy due to its shear strength. Thus the very large Phase B may have spent its energy on the slope and come to an equilibrium without catching up with and influencing the movement on the lower slope. Under Scenario 1, the distal Phase A initiated the landslide and produced the damage, but was essentially completed by the time the proximal Phase B descended behind it to the river channel. Under Scenario 3, Phase B initiated the movement, but came to an equilibrium on the midslope. Although little energy was transmitted to the colluvial accumulations, rapid undrained loading destabilized this material and caused its own failure. Given the extreme strength loss connected with spontaneous liquefaction of the softened colluvium, the resulting Phase A released even more energy and produced the disastrous damage on the south side of the river. Under Scenario 2, both phases may have occurred simultaneously, yet little energy was transmitted between them because the distal phase was more mobile than the proximal phase.

Evidence that relatively little energy was transmitted between the two motion phases can be observed near a *contact line* just to the south of the present river channel (Fig. 7). The zone of debris

Fig. 7. Contact line separating debris involved in Phase A (upper part of the figure) and Phase B (map data: Google, Landsat/Copernicus)

adjacent to the contact line is among the thinnest parts of the debris field (this is why the river overflowed the debris at this point). The morphology of the debris in this area shows no evidence of high compressional stresses having been transmitted through the zone such as faults, thickening or pressure ridges. On the contrary, the relatively smooth debris surface with shallow depressions is indicative of longitudinal extension and thinning. In Scenario 1, the contact zone represents the line where the leading front of Phase B arrived to overrun the previously deposited and now stationary debris of Stage A at the present location. In Scenario 3, the contact line may have formed on the lower slopes, as the toe of Phase B came to rest at the head of the colluvial accumulations. When the latter subsequently failed and a flowslide extended farther, the contact line with its toppled trees was transported downslope to its present position on the floor of the valley. In neither case was significant force (and energy) transmitted by compression from Phase B to Phase A. Therefore the temporal sequence of the movement phases has little effect on the results of the dynamic analysis.

Failure Surface Reconstruction

Reconstructing the failure surface is a difficult step in the dynamic analysis of the Oso landslide. A portion of this surface is visible in the main scarp, but the rest of the failure surface is obscured by slide debris. Therefore a large part of the surface on which the failed mass moved must be inferred from field evidence. The primary source of data used to reconstruct the failure surface is the morphology of the deposits, as observed on the pre-event and postevent LiDAR topography data, as well as four boreholes drilled by the Washington Department of Transportation (WSDOT) (Badger 2015).

The geometry of the Phase A failure surface was chosen to correspond with the mechanism described in Stark et al. (2017), in which a relatively small initial failure in the upper part of the slope induces a large strength loss in the colluvium accumulated at the toe of the slope. Multiple pieces of evidence support this interpretation. As discussed previously, the measured area of intact blocks of forest floor rafted onto the valley indicates that the valley floor deposits derived primarily from material originally located to the southeast of the Whitman Bench. In its prefailure position, this material was traversed by two scarps: the scarp associated with the ancient landslide and the scarp associated with the 2006 landslide. The locations of these scarps correspond to the dropped-down slabs of material identified in the 2014 debris field (Fig. 5),

© ASCE   05017005-5   J. Geotech. Geoenviron. Eng.

J. Geotech. Geoenviron. Eng., 2017, 143(9): 05017005

indicating that the material originally located between the scarps and the 2013 ground surface was displaced during the flowslide. Therefore, both the ancient and 2006 scarps were used as the back scarp of the Phase A failure surface (Fig. 1). The 2013 LiDAR showed a thick accumulation of colluvium from the toe of the slope to the river derived from the 2006 and other landslides. This colluvium is assumed to have undergone a substantial amount of strength loss during the Phase A failure, so the rupture surface was chosen to correspond to the 2003 ground surface in this section.

The Phase B failure surface was interpreted as a compound surface with a nearly horizontal plane located in the glaciolacustrine unit (Fig. 1). A large intact block came to rest in the source zone of Phase A, although it was deformed along multiple inclined shears. The style of this deformation is indicative of a nearly horizontal plane located in the glaciolacustrine unit, typical of a bilinear compound slide (Hutchinson 1988). In front of this intact block, slabs of material *scalloped* or dropped down, exhibiting marked extension while moving over a steeply inclined steplike surface segment (Fig. 5).

The elevation of the nearly horizontal planes in the upper glaciolacustrine unit can be inferred from the four WSDOT boreholes (Fig. 2). In EB-04si-15 the elevation of the rupture surface was determined by the contact between a sandy unit (likely galciofluvial) and a silt/clay unit (likely glaciolacustrine). In H-12si-15 the borehole log noted variably inclined partings at an elevation of approximately 105 m. In EB-07si-15 and EB-09si-15 borehole logs indicated slickensides/disruption at elevations of 105 m.

Because the proposed failure surface was based partly on indirect evidence, some uncertainty is associated with it. However, compared with the failure surfaces proposed by other researchers (Wartman et al. 2016; Keaton et al. 2014; Iverson et al. 2015), it appears to be the most consistent with field observations and site conditions. For example, varved silt and clay is expected to have anisotropic strength properties. This, combined with evidence of strong internal distortion of the source volume, as well as the observation that there was little elevation change between the 2013 and 2014 LiDAR surveys southeast of the large intact block in the source zone (Fig. 6), negates the possibility that the failure surface was circular (Wartman et al. 2016; Keaton et al. 2014) or a logarithmic spiral (Iverson et al. 2015). The proposed compound surface agrees with field observations as well as the expected failure behavior of the overconsolidated upper glaciolacustrine unit, and corresponds to the positions of shear surfaces identified in the 2015 drillholes (Badger 2015).

Hibert et al. (2015) estimated that the volume of the Phase B debris was 25% that of the Phase A debris, which contradicts the interpreted rupture surface in Fig. 1. The Hibert et al. (2015) estimate was based on the assumption that the peak acceleration of the centers of mass of the Phase A and Phase B material were the same. The results of the present paper suggest that this assumption is not appropriate, and that the acceleration of the Phase A material was significantly greater than that of the Phase B material.

Description of Dynamic Models

The two dynamic models used herein were DANW and its 3D extension DAN3D, which were described in detail by McDougall (2006) and Hungr and McDougall (2009). These models are depth-averaged numerical solutions of the equations of motion in one and two dimensions. The solutions are implemented in a Lagrangian framework without a fixed mesh and implement the Savage–Hutter (1989) assumptions regarding nonhydrostatic internal stress distribution. The equations of motion solved by these models are shown in Eqs. (1) and (2)

$$\rho h \frac{Dv_x}{Dt} = \rho h g_x - k_x \sigma_z \frac{\partial h}{\partial x} + \tau_{zx} - \rho E v_x \tag{1}$$

$$\rho h \frac{Dv_y}{Dt} = \rho h g_y - k_y \sigma_z \frac{\partial h}{\partial y} \tag{2}$$

where ρ = density; $v_{x,y}$ = depth-averaged x and y velocities; h = flow depth; $g_{x,y}$ = x and y components of gravity; $k_{x,y}$ = x and y horizontal stress ratios (ratio of lateral stress to bed-normal stress); σ_z = bed-normal stress; τ_{zx} = basal resistance; and E = entrainment rate. The basal resistance entrainment terms only occur in the x-direction because DAN3D aligns the coordinate system of each fluid parcel with its local direction of motion. Because DANW is a 2D model, only Eq. (1) is solved. DAN3D uses the smooth particle hydrodynamics solution method to solve the governing equations (Monaghan 1992).

The models use an open rheological kernel, allowing for the use of a variety of rheological relationship to describe the dependency of basal shear resistance on depth and velocity. When performing an inverse analysis with DAN3D, the parameters that are commonly calibrated are the internal angle of friction of the failed material and the parameters associated with the user-specified basal rheology. The ability of the models to entrain material during motion was not utilized in the present case.

Model Rheology

After a considerable amount of trial-and error testing using several rheologies, the basal resistance to sliding was parameterized using two different rheological models. The boundaries between the two rheologies are shown in Fig. 1. The basal shear resistance experienced by Slide Mass #1 (labeled A in Fig. 1) was evaluated using the *liquefied* rheology. The basal resistance experienced by Slide Mass #2 (labeled B in Fig. 1) was calculated using the frictional rheology with a constant apparent friction angle and pore-water pressure ratio.

An assumption implicit in this analysis was that the Phase B material did not contain or override liquid material. The source zone contains a nearly intact but heavily sheared block, with massive blocks dropped down over the step in the rupture surface (Fig. 5). The intact morphology of this material suggests that no part of it experienced a large undrained strength loss, i.e., liquefaction, during its motion.

To simulate the liquefied part of the Oso landslide in Phase A, a new rheology was implemented into DANW and DAN3D. This rheology was called the *liquefied rheology* and was based on the work of Stark and Mesri (1992) and Olson and Stark (2002), which normalized the liquefied shear strength with the initial vertical effective stress acting at the onset of failure. Olson and Stark (2002) compiled a database of 33 liquefaction flow failures in loose, saturated granular materials. The liquefied strength ratio is a ratio of the liquefied strength to the prefailure vertical effective stress. Once the liquefied strength of the material is determined under this assumption, this strength is assumed to remain constant for the duration of flow, corresponding to undrained (constant volume) conditions. In granular materials, the liquefied strength ratio can be estimated using the standard penetration test blow count or cone penetrometer tip resistance, which are both measures of initial material density.

Because the blow count for the heterogeneous colluvial material that failed in the Oso landslide is unknown, a representative value

of the ratio of liquefied strength to prefailure effective stress of 0.07 was selected for a trial flow analysis. This rheology was implemented into DANW and DAN3D using Eq. (3)

$$s_l = 0.07 \times (\sigma_v - u) \qquad (3)$$

where s_l = liquefied shear strength; σ_v = prefailure vertical total stress; and u = prefailure pore pressure.

In its current form, the basal resistance used with the liquefied rheology has no dependence on shear rate, i.e., it is a constant purely plastic strength. Rate-dependent resistance may be included in the future by incorporating the liquefied shear strength into the Herschel–Bulkley rheology, in a manner similar to De Blasio et al. (2011). However, the velocities obtained in the analysis were not unrealistically high and the introduction of rate dependence did not seem to be essential. The analyses that follow assumed that the flow experienced only negligible viscous or turbulent resistance.

During the first time step of both the 2D and 3D analyses, the initial vertical effective stress on each element was calculated based on an assumed unit weight and pore-water pressure ratio, and the liquefied strength of that element was calculated based on Eq. (3). When the liquefied rheology is used, the basal shear strength is independent of total stress changes, which differentiates it from the frictional and Voellmy rheologies commonly used to analyze extremely rapid flowlike landslides (e.g., Hungr and McDougall 2009). The Bingham rheology (e.g., Jeyapalan 1981) assumes a constant yield strength; however, unlike the liquefied rheology, this strength is constant and independent of prefailure vertical effective stress.

In contrast to the model by Iverson et al. (2015), drainage (consolidation) of the high pore-water pressure in the liquefied soil during motion was not considered in the analysis. This was because orderly diffusion of fluid pressure probably could not occur in the rapidly flowing saturated mass, where drainage paths are constantly interrupted by mixing. Furthermore, even if the soil were coarse, the timescale for significant drainage would be longer than the short period required for the emplacement of the debris.
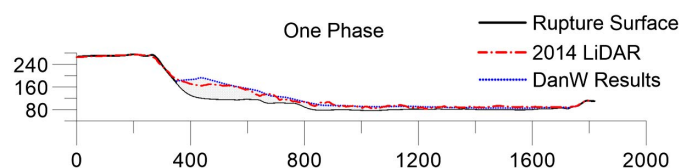
Simulation Results

2D Simulations

Fig. 8 summarizes the results of the 2D simulations, in which the two phases were assumed to be separated by a time gap. In particular, Fig. 8 shows a comparison between the final surface predicted by DANW and that derived from the 2014 LiDAR. Comparison of these two surfaces shows that DANW was able to reproduce the runout distance and deposit distribution. The blocky nature of the debris was not reproduced because DANW models the sliding mass as a homogeneous material. The distal end of the deposit was also thinner than indicated on the 2014 LiDAR, likely due to the neglect of rate-dependent resistance and entrainment of debris and vegetation by the flow front. A bulk friction angle of 12°, consistent with residual friction angles measured by Stark et al. (2017), was used to simulate the Phase B material.

Fig. 9 shows the results of 2D simulations, in which no time gap was simulated between the two phases. The results, in terms of runout distance and deposit distribution, were nearly identical to those determined for the simulations in which the phases moved separately. The similarity between the two sets of simulations demonstrates that the observed deposit shape was not controlled by the temporal sequence of failure but instead by the distribution of shear strength along the failure surface. The large intact block deposited
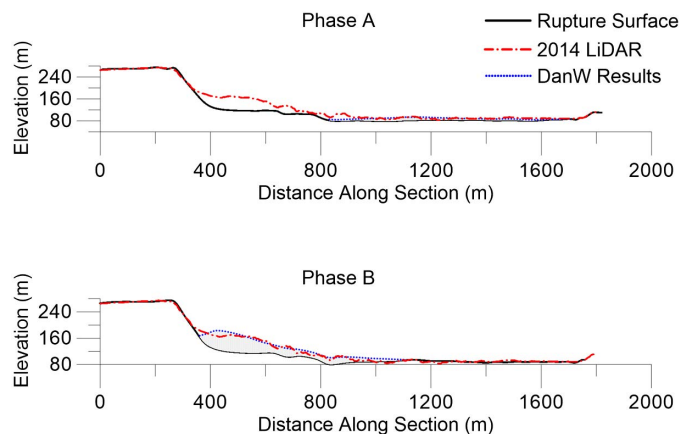
Fig. 8. Simulated flow depths for Phases A and B; results show good agreement with the deposit depths derived from the 2014 LiDAR
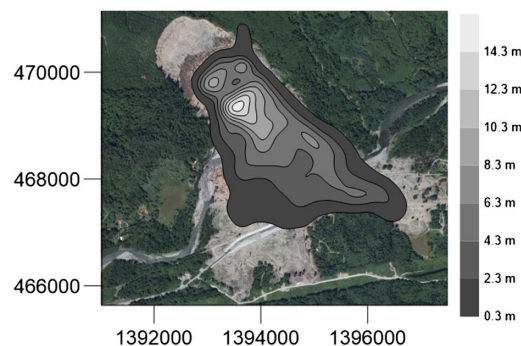

Fig. 9. Simulated flow depths for DANW simulations that assume no time gap between the two phases; results are similar to Fig. 8

in the source zone was well reproduced because this material had a higher strength and remained frictional.
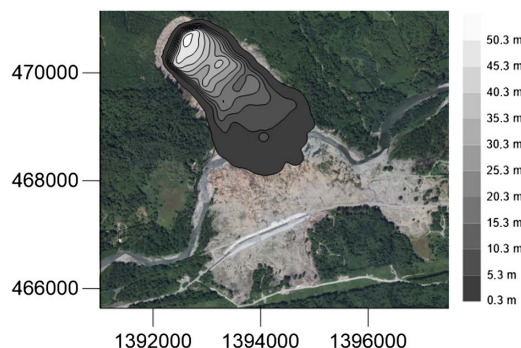
3D Simulations

Figs. 10 and 11 show the final deposit depths predicted by the 3D simulations for Phase A and Phase B, respectively. These results cannot be directly compared with Fig. 6 because these deposit depths were calculated based on the difference in elevation between the top of the deposit and the failure surface, whereas accumulation and depletion maps were calculated based on the difference between the pre-event ground surface and the top of the slide deposit. In areas where material was removed and then partially replaced, such as the source zone, deposit depths will be positive but the map will show depletion. To better facilitate comparisons between model results and field observations, a map showing the zones of accumulation and depletion predicted by DAN3D was created by adding the calculated deposit depths to the map of the failure surface and sliding/flow path (Fig. 12). These simulations treated the failure as two discrete events, using the same parameters as used in the 2D analyses. The model adequately reproduced the impact area and deposit distribution. Similar to the 2D analyses, the distal end of the predicted deposit was thinner than that observed in the field, for reasons stated previously. The model did not reproduce the deposits in the southwest corner (the *splash* area) because these deposits represent a small volume of material entrained in the valley that mixed with surface water and was projected ahead of the main debris mass. This process was not simulated with the present dynamic models.

To further verify the 3D simulations, the 3D model was used to simulate the structural damage caused by the 2014 landslide. For this purpose, the model results were used to derive the *debris flow vulnerability index* proposed by Jakob et al. (2012). This empirical

© ASCE 05017005-7 J. Geotech. Geoenviron. Eng.

J. Geotech. Geoenviron. Eng., 2017, 143(9): 05017005

Fig. 10. Results of DAN3D simulation of first phase of movement with impact area and deposit distribution in agreement with field observations; no effort was made to reproduce the splash zone (background image courtesy of Esri Disaster Response Program and WSDOT)


Fig. 11. Results of DAN3D simulations of Phase B overlaid on post–2014 event orthophotograph; the simulated deposits extend to the contact zone (background image courtesy of Esri Disaster Response Program and WSDOT)
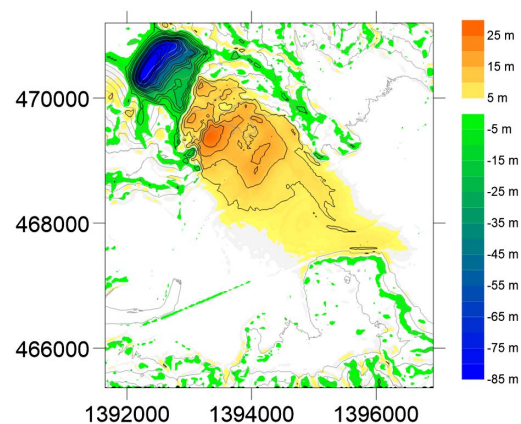

Fig. 12. Accumulation and depletion zones predicted by DAN3D; the splash zone was not modeled, so the impact area in the western section is less than that observed

index was correlated to structural damage for a wide variety of case histories of damaging debris flows. It is calculated with Eq. (2) where li_{df} = debris flow impact index; h = flow depth; and v = velocity

$$li_{df} = h \times v^2 \qquad (4)$$
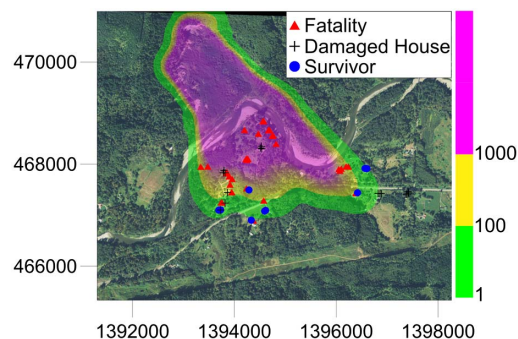
Fig. 13. Model-simulated intensity index compared with building damage; the units of intensity index are m³ s⁻²; according to Jakob et al. (2012), values of the intensity index between 1 and 100 m³ s⁻² correspond to some/major structural damage, values from 100 to 1,000 m³ s⁻² correspond to major structural damage/complete destruction, and values greater than 1,000 m³ s⁻² indicates complete destruction (background image from National Agriculture Imagery Program, data available from the U.S. Geological Survey)
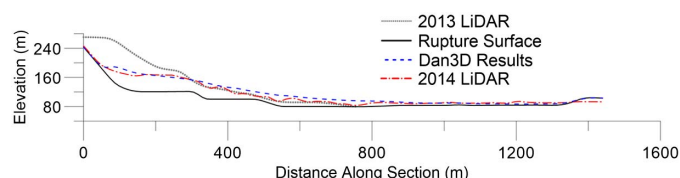
Fig. 14. Representative cross section through the DAN3D results showing the simulated deposit depths; the results are in good agreement with the deposit surface derived from the 2014 LiDAR
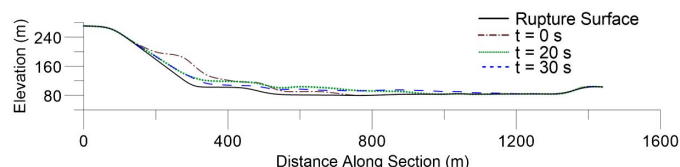
Fig. 15. Sections through the DAN3D Phase A simulation at 10-s intervals showing slide debris piling up at the slope toe before spreading over valley floor

Values of the impact index greater than 100 usually result in complete destruction of weak structures, whereas values between 10 and 100 tend to result in major structural damage (Jakob et al. 2012). Fig. 13 shows the maximum value of the impact index calculated by the DAN3D model, compared with the locations of houses in the deposit zone. Model estimates of the impact index correlate well with those inferred from field evidence, suggesting that the spatial distribution of the simulated velocities and depths is realistic.

Fig. 14 shows a representative cross section through the 3D model results. The model was able to reproduce the deposit distribution derived from the 2014 LiDAR data. Comparing Fig. 14 with Fig. 8 shows that the DANW and DAN3D results are nearly identical. Fig. 15 shows cross sections through the 3D model results at different times during the motion.

© ASCE   05017005-8   J. Geotech. Geoenviron. Eng.

J. Geotech. Geoenviron. Eng., 2017, 143(9): 05017005

Discussion

The two dynamic models used herein were able to reproduce key field observations from the 2014 Oso landslide with a reasonable degree of accuracy. The successful simulations suggest that the reconstructed rupture surface is plausible, and that the hypothesized distribution of frictional and liquefied shear strength can explain the field observations related to the mobility of this event. Furthermore, the exact temporal sequencing of the two failure phases had little effect on the results of the dynamic analyses because there was little energy transmitted through the thin extensional contact zone between the two phases.

Because inverse analysis was used to determine the shear strengths, the results are likely nonunique. For the Phase A simulations, multiple combinations of pore-pressure ratio and liquefied strength ratio can lead to similar simulation results. However, it is likely that the colluvium was saturated prior to catastrophic failure. This restricts the range of possible pore pressure ratios, and consequently the range of best-fit liquefied strength ratios.

The hypothesized failure mechanism differed from that published by Iverson et al. (2015) and Iverson and George (2016), who assumed that the entire source volume of the 2014 landslide, including both the pre-existing colluvial deposits and the intact glacial, glaciofluvial, and glaciolacustrine soils liquefied during failure. The resulting simulations by Iverson et al. (2015) and Iverson and George (2016) predicted that no material would deposit in the source zone, and a thick (∼30 m) deposit was simulated at the distal end of the debris. This does not correspond to observations, as shown clearly by Fig. 6.

In this analysis, the debris from the Whitman Bench did not experience near-zero strength, and as a result a large volume of debris remained in the source zone and the deposit on the valley floor was much thinner. The hypothesized mechanism provides a better explanation of the available field evidence, because boreholes have demonstrated a thick accumulation of deposits in the source zone (Badger 2015), and accumulation/depletion maps indicate that the valley floor deposit is thin.

Based on the dynamic analysis, the following constraints on the motion of the Oso landslide can be inferred:
1. The failure initiated from the top of the slope.
2. The two phases of motion were defined by a change in the rheology of the failed mass. The debris that attained extremely rapid velocities and caused most of the damage (Phase A) was much weaker than the material deposited in the proximal part of the deposit. The Phase B failure of the Whitman Bench did not have a significant influence on the mobility of the distal debris.
3. The dynamics of the mobile phase of the event were driven by large internal pressure gradients, facilitated by near zero basal shear resistance.

That the failure occurred from the top of the slope, as opposed to the bottom, is significant because it excludes any possibility of river erosion having triggered this landslide (Stark et al. 2017). Some of the previous landslides on this site likely were triggered by erosion at the toe of the slope due to the river (Stark et al. 2017). The 2014 event represents a distinct mechanistic change from the recent (last 100 years) behavior of this slope.

The large undrained strength loss, i.e., liquefaction, of the saturated colluvium along the slope toe occurred partly by undrained loading, as the mass of the initial slide from above landed on the loose soil (Stark et al. 2017). However, the greater part of the liquefied volume likely was not overridden. Its liquefaction therefore must have occurred spontaneously, as a result of deformation and rapidly applied shear stresses caused by the initial failure. The authors visualize such liquefaction as a chain process as illustrated in Stark et al. (2017) using concepts from Sassa (1985). This process requires a certain critical input of released energy to propagate the strength loss to the entire volume of the flow.

The distribution of shear strength is significant because it demonstrates that the debris that caused the damage presented little resistance to sliding. It also shows that the failure of the Whitman Bench, which was determined to have relatively high strength, did not significantly influence the motion of the low-strength debris. The behavior of this catastrophic landslide was the same regardless of whether the mass failed as one single event or as two temporally distinct events. The key to understanding why this slope failed as it did is understanding the mechanism of significant strength loss in the material of the distal phase of the event.

The analysis presented in this paper does not provide a mechanistic description of the process of strength loss because the strengths were estimated from an inverse analysis. However, this analysis shows that to reproduce the runout distance and velocities observed for the 2014 landslide, the leading edge of the debris, likely consisting of saturated colluvium from previously failed deposits, must have experienced a dramatic undrained strength loss and/or liquefied. Overconsolidated, insensitive glaciolacustrine silt and clay is not commonly recognized as being susceptible to liquefaction. The process that led to the liquefaction of this colluvial material is the key to understanding why this slide mass moved more than 1.4 km.

Comparison with Prior Case Histories

Based on an in-depth analysis of the Attachie flowslide in northeastern British Columbia in 1975, Fletcher et al. (2002) attempted to explain the inferred strength loss of an overconsolidated, insensitive glaciolacustrine silt and clay. Fletcher et al. (2002) hypothesized that loosening and softening of previously failed blocks of overconsolidated silt and clay can be followed by infilling of joints between the blocks by loose, low hydraulic–conductivity sediments and water. This material would then be susceptible to a process similar to nonseismic undrained strength loss, i.e., spontaneous liquefaction, if subjected to a sufficiently strong deformation under undrained conditions. The liquefied mass would then flow, carrying fragments of *intact* original soil within and on top of the flow. The 2014 Oso landslide displayed many similarities with the Attachie slide, including similar material types and site history. Loosening and softening of exposed clay surfaces has been documented to trigger earthflows at the Oso landslide site (Shannon and Wilson 1952), although the scale of the phenomenon was not large enough to induce liquefaction.

Another possible mechanism that could explain the low strength from inverse analyses could be the loss of cohesion in a lightly cemented and saturated silt layer of the upper glaciolacustrine unit. This process was documented by Conlon (1966) at the Toulnustouc flowslide that occurred in 1966 in Quebec. Such a process might be used as an alternative explanation of the 2014 Oso landslide because it is conceivable that a loss of cohesion in a silt layer could cause material to rapidly vacate the source zone, leading to rapid undrained loading of saturated colluvium derived from previous landslides, as occurs in many debris avalanches (Hungr et al. 2014). Such a landslide would have to occur in a single phase, although there would still be a difference in the character of the blocky proximal and liquid distal deposits. However, the cemented silt at Toulnustouc was clearly identifiable as extremely sensitive (Conlon 1966), whereas sensitive material has not been found in the site investigation documents or samples tested to date from the 2014 Oso landslide.

Both of these mechanisms require the presence of low-plasticity silt beds, the brittle failure of which can lead to rapid strength loss.

Furthermore, the macroscopic brittleness mechanism requires large accumulations of previously failed material. Low-plasticity silt varves were identified in the upper glaciolacustrine unit (Stark et al. 2017), and there appears to be an abundance of previously failed material derived from prehistoric and historic landslides along the lower portion of the slope. Therefore, these mechanisms are conceivable, and independently or together can be used to explain the observed strength loss. Further research is required to definitively conclude that one or both of these mechanisms was responsible for the simulated strength loss in the dynamic analyses presented herein.

Summary

The dynamic analysis presented herein and validated by field evidence demonstrates that the 2014 Oso landslide occurred in two phases, defined not as much by the timing sequence but primarily by a large difference in the shear strength along large portions of the failure surface. The material that moved in the distal Phase A of motion was primarily composed of liquefied colluvium derived from previous low-elevation landslides. The high mobility of the liquefied debris was the primary cause of the disastrous damage in Steelhead Haven. This paper suggests two mechanisms to explain this strength loss: macroscopic brittleness due to softening of mechanically disturbed debris (colluvium) and the presence of saturated silt beds. Both of these mechanisms require the presence of a softened, saturated colluvial mass to explain the dramatic runout. Hazard mapping of similar slopes should focus on identifying the presence of such colluvial masses at the toe of high slopes.

Acknowledgments

Notation

The following symbols are used in this paper:

h = flow depth;
li_{df} = debris flow impact index;
s_l = liquefied shear strength;
u = prefailure pore pressure;
v = depth averaged velocity; and
σ_v = vertical total stress.

References

Badger, T. C. (2015). "Geotechnical report: SR 530 MP 35 to 41 geotechnical study." Washington Dept. of Transportation, Olympia, WA, 199.

Conlon, R. (1966). "Landslide on the Tolnustouc River, Quebec." *Can. Geotech. J.*, 3(3), 113–144.

De Blasio, F. V., Breien, H., and Elverhøi, A. (2011). "Modelling a cohesive-frictional debris flow: An experimental, theoretical, and field-based study." *Earth Surf. Processes Landforms*, 36(6), 753–766.

Dragovich, J., Stanton, B. V. W., Lingley, W. S., Jr., Briesel, G. A., and Polenz, M. (2003). "Geologic map of the Mount Higgins 7.5-minute Quadrangle, Skagit and Snohomish Counties, Washington." *Open File Rep. 2003–12*, Washington Divisions of Geology and Earth Resources, Olympia, WA.

Fletcher, L., Hungr, O., and Evans, S. G. (2002). "Contrasting failure behavior of two large landslides in clay and silt." *Can. Geotech. J.*, 39(1), 46–62.

Heim, A. (1932). *Bergsturz und Menschenleben [Landslides and human lives]*, Bitech Press, Vancouver, BC, Canada.

Hibert, C., Stark, C. P., and Ekström, G. (2015). "Dynamics of the Oso-Steelhead landslide from broadband seismic analysis." *Nat. Hazards Earth Syst. Sci.*, 15(6), 1265–1273.

Hungr, O., Leroueil, S., and Picarelli, L. (2014). "The Varnes classification of landslide types, an update." *Landslides.*, 11(2), 167–194.

Hungr, O., and McDougall, S. (2009). "Two numerical models for landslide dynamic analysis." *Comput. Geosci.*, 35(5), 978–992.

Hutchinson, J. N. (1988). "General report: Morphological and geotechnical parameters of landslides in relation to geology and hydrogeology." *Proc., 5th Int. Symp. on Landslides*, A.A. Balkema, Rotterdam, Netherlands, 3–35.

Iverson, R. M., et al. (2015). "Landslide mobility and hazards: Implications of the 2014 Oso disaster." *Earth Planet. Sci. Lett.*, 412, 197–208.

Iverson, R. M., and George, D. L. (2016). "Modelling landslide liquefaction, mobility bifurcation and the dynamics of the 2014 Oso disaster." *Géotechnique*, 66(3), 175–187.

Jakob, M., Stein, D., and Ulmi, M. (2012). "Vulnerability of buildings to debris flow impact." *Nat. Hazard.*, 60(2), 241–261.

Jeyapalan, K. (1981). *Analysis of flow failures of mine tailings impoundments*, Univ. of California, Berkeley, CA.

Keaton, J. R., et al. (2014). "The 22 March 2014 Oso landslide, Snohomish County, Washington." *Rep. No. GEER-036*, Geotechnical Extreme Event Reconnaissance, National Science Foundation, Arlington, VA, 228.

McDougall, S. (2006). "A new continuum dynamic model for the analysis of extremely rapid landslide motion across complex 3D terrain." Ph.D. thesis, Univ. of British Columbia, Vancouver, BC, Canada.

Miller, D. (1999). "Hazel/Gold Basin landslides: Geomorphic draft report." U.S. Army Corps of Engineers, Washington, DC, 26.

Monaghan, J. (1992). "Smoothed particle hydrodynamics." *Ann. Rev. Astron. Astrophys.*, 30(1), 543–574.

Olson, S., and Stark, T. D. (2002). "Liquefied strength ratio from liquefaction flow failure case histories." *Can. Geotech. J.*, 39(3), 629–647.

Sassa, K. (1985). "The mechanism of debris flow." *Proc., 11th Int. Conf. on Soil Mechanics and Foundation Engineering (SMFE)*, Vol. 2, San Francisco, 1173–1176.

Savage, S. B., and Hutter, K. (1989). "The motion of a finite mass of granular material down a rough incline." *J. Fluid Mech.*, 199, 177–215.

Shannon, W. D., and Wilson, (1952). "Report on slide on North Fork Stillaguamish River near Hazel, Washington." State of Washington Dept. of Game and Fisheries, Arlington, VA, 18.

Stark, T. D., Baghdady, A., Hungr, O., and Aaron, J. (2017). "Case study: Oso landslide on 22 March 2014—Material properties and failure mechanism." *J. Geotech. Geoenviron. Eng.*, 10.1061/(ASCE)GT.1943-5606.0001615, 05017001.

Stark, T. D., and Mesri, G. (1992). "Undrained shear strength of liquefied sands for stability analysis." *J. Geotech. Eng.*, 10.1061/(ASCE)0733-9410(1992)118:11(1727), 1727–1747.

Wartman, J., et al. (2016). "The 22 March 2014 Oso landslide, Washington, USA." *J. Geomorphol.*, 253(1), 275–288.

© ASCE   05017005-10   J. Geotech. Geoenviron. Eng.

J. Geotech. Geoenviron. Eng., 2017, 143(9): 05017005